Journal of Thermal Analysis and Calorimetry (2025) 150:15817–15830
https://doi.org/10.1007/s10973-025-14774-9

Heat transfer optimization and sensitivity analysis of ternary hybrid nanofluid flow over a moving surface with joule heating

Umi Nadrah Hussein[1] · Najiyah Safwa Khashi'ie[1] · Mohd Fariduddin Mukhtar[2] · Norihan Md Arifin[3] · Ioan Pop[4]

Received: 4 May 2025 / Accepted: 29 August 2025 / Published online: 26 September 2025

Abstract

Efficient heat transfer is a major challenge in systems like MHD pumps, electromagnetic cooling units and rotating heat exchangers especially under extreme conditions. The combined effects of magnetic fields, Joule heating and multiple nanoparticles create complex behaviors that are hard to solve using analytical methods. Therefore, reliable numerical methods and statistical optimization tools are needed to analyze and improve these systems. Hence, this work highlights ternary hybrid nanofluid flow over a permeable moving surface with the influence of magnetohydrodynamic (MHD), Joule heating and suction effects, integrating both computational and optimization techniques. The fluid comprises water-based ternary hybrid nanofluid containing aluminum oxide (Al_2O_3), copper (Cu) and titanium dioxide (TiO_2) nanoparticles. The governing partial differential equations are transformed into a system of ordinary differential equations using similarity transformations and solved using the bvp4c solver (MATLAB). Validation of the numerical approach is carried out by comparing results with existing literature which showing excellent agreement for limiting cases. Response surface methodology (RSM) is applied to analyze interactions between the key parameters. Results indicate that both magnetic parameter and titania concentration significantly enhance the velocity profile due to the induced Lorentz force and altered thermal gradient. Analysis of variance (ANOVA) confirms that magnetic parameter and titania concentration are the most influential on thermal and flow responses. Sensitivity analysis further highlights strong linear and interaction effects.

Keywords Joule heating · Magnetohydrodynamics · Moving surface · Response surface methodology · Sensitivity analysis · Ternary hybrid nanofluid

Abbreviations

B_0	Strength of the magnetic field (constant)
B	Magnetic field function
C_f	Skin friction coefficient
C_p	Specific heat at constant pressure/$Jkg^{-1}K^{-1}$
Ec	Eckert number
k	Thermal conductivity of the fluid/$Wm^{-1}K^{-1}$
M	Magnetic parameter
Nu_x	Local nusselt number
Pr	Prandtl number
Re_x	Local reynolds number
r_0	An intercept term
r_A, r_B, r_C	Linear term reflecting individual parameter effect
$r_{A^2}, r_{B^2}, r_{C^2}$	Quadratic terms capturing nonlinear responses
r_{AB}, r_{BC}, r_{CA}	Interaction terms describing the coupled influences between variables
S	Suction parameter
T_w, T_∞	Temperature of the surface and surrounding, respectively/K
T	Temperature of the ternary hybrid nanofluid/K
U	Constant of free-stream velocity/ms^{-1}
u, v	Velocity component in the x- and y- directions, respectively/ms^{-1}
v_w	Wall mass velocity/ms^{-1}
x, y	Cartesian coordinates/m

✉ Najiyah Safwa Khashi'ie
najiyah@utem.edu.my

[1] Fakulti Teknologi Dan Kejuruteraan Mekanikal, Universiti Teknikal Malaysia Melaka, Hang Tuah Jaya, Durian Tunggal, 76100 Melaka, Malaysia

[2] Fakulti Pengurusan Teknologi Dan Teknousahawanan, Universiti Teknikal Malaysia Melaka, Hang Tuah Jaya, Durian Tunggal, 76100 Melaka, Malaysia

[3] Department of Mathematics and Statistics, Faculty of Science, Universiti Putra Malaysia UPM, 43400 Serdang, Selangor, Malaysia

[4] Department of Mathematics, Babeş-Bolyai University, 400084 Cluj-Napoca-Napoca, Romania

Greek symbols

λ	Velocity ratio parameter
σ	Electrical conductivity
ψ	Stream function
η	Similarity variable
μ	Dynamic viscosity of the fluid/kgm^{-1}s^{-1}
ν	Kinematic viscosity of the fluid/m^{2}s^{-1}
ρ	Fluid density/kgm^{-3}
ϕ_1,ϕ_2,ϕ_3	Volumetric concentrations of Al_2O_3, Cu and TiO_2, respectively

Subscripts

f	Base fluid
nf	Single nanofluid
thnf	Ternary hybrid nanofluid
s_1,s_2,s_3	Solid component for the Al_2O_3, Cu and TiO_2, respectively

Superscript

′	Differentiation with respect to η

Introduction

The ability of fluids to conduct and dissipate heat efficiently is essential in numerous engineering and industrial processes where accurate thermal regulation is key to sustaining optimal system performance. Choi and Eastman [1] pioneered the development of nanofluids which involve the suspension of nanoscale particles within a conventional base fluid to significantly improve the fluid's thermal conductivity and overall heat transfer performance. Since that, nanofluids have been the focus of extensive research and have found diverse applications in high-efficiency systems such as heat exchangers, microelectronic cooling technologies, automotive thermal management and solar thermal collectors. Very recent, Kamal et al. [2] applied second law analysis to investigate the two-phase Maxwell nanofluid flow with Marangoni convection and gyrotactic microorganisms over a rotating disk. Other studies on the thermal performance of single nanofluids were conducted by Reddy et al. [3, 4] and Shah et al. [5]. Driven by the growing need for enhanced heat transfer capabilities, researchers have progressed from single nanofluids to the development of hybrid nanofluids, which combine 2 different types of nanoparticles to achieve improved thermal conductivity and flow behavior. Li et al. [6] performed a parametric simulation of magnetohydrodynamics couple stress hybrid nanofluid flow (combination of silver and black iron oxide nanoparticles with vacuum pump oil) in the presence of Joule heating and heat radiation effects. Meanwhile, Ahmad et al. [7] observed that the heat transfer enhancement of Casson hybrid nanofluid flow was up to 19.71% as compared to the Casson nanofluid with single nanoparticle which was only capable to enhance up to 9%. Both Ali et al. [8] and Shah et al. [9] applied Laplace transform technique for analyzing the heat and flow progresses of the hybrid nanofluid flow. On the other hand, Gireesha et al. [10], Manvitha et al. [11] and Lakshmi et al. [12] used either Taylor or Hermite wavelet approach to solve their hybrid nanofluid flow cases. Interestingly, these wavelet techniques are not limited for nanofluid cases and also can be used in analyzing various fluid flow problems as discussed by Gireesha et al. [13] (Taylor wavelet), Manvitha et al. [14] (Fibonacci wavelet) and Gowtham et al. [15] (Tricomi–Carlitz wavelet). Other recent findings regarding boundary layer flow of hybrid nanofluid can also be found in Kamal et al. [16], Zuberi et al. [17, 18] and Zainal et al. [19].

This advancement has then led to the emergence of ternary hybrid nanofluids, integrating three distinct nanoparticles to harness synergistic thermal characteristics. Both computational and experimental investigations such as those conducted by Xuan et al. [20] have confirmed the superior thermal performance of ternary hybrid nanofluids, making them highly suitable for high-efficiency thermal management in industrial applications. However, there are still limited numerical studies which highlighted the flow behavior and thermal progress of ternary hybrid nanofluids subjected to few surfaces such as stretching/shrinking plate (see Jamrus et al. [21–25]) and cylinder (see Hussein et al. [26, 27], Mahboobtosi et al. [28] and Patil et al. [29]) and channel (see Murtaza et al. [30] and Lakshmi et al. [31]).

Joule heating in theory describes the conversion of electrical energy into thermal energy due to resistive dissipation within a medium. This phenomenon is fundamental in the operation of various electrical and electronic systems. In the context of boundary layer flow, Joule heating serves as a crucial control parameter for elevating the thermal state of nanofluids, as reported by Reddy and Reddy [32]. The influence of this mechanism on the thermal behavior of Cu–Al_2O_3/water nanofluid has been explored in different geometric setting specifically over stretching and shrinking cylinders as studied by Maskeen et al. [33] and Khashi'ie et al. [34], respectively. In the latter study, it was revealed that the dimensionless Eckert number, which quantifies the effect of Joule heating, does not contribute to delaying the separation point which consistent with the observations of Yan et al. [35]. Further investigation into magnetohydrodynamic (MHD) hybrid nanofluid flow incorporating both Joule heating and thermal radiation effects was carried out by Chamkha et al. [36], focusing on the configuration between two parallel plates. These studies underscore the importance of considering Joule heating in thermal analysis and design, especially in electrically conductive nanofluid systems under MHD influences. Khashi'ie et al. [37] analyzed the simultaneous effects of magnetic field and Joule heating on the free-stream flow of hybrid nanofluid subjected to moving plate. They found that the dual solutions only exist on limited range of the moving parameter. Li et al. [38] analyzed the effect of Joule heating on nanofluid flow through a permeable duct, highlighting its role in altering temperature distributions and flow behavior. Saranya et al. [39] examined the combined influence of viscous dissipation and Joule heating on hybrid ferrofluid flow over a contracting cylinder. In their investigation, a mixture of magnetite and cobalt ferrite nanoparticles was suspended in a binary base fluid composed of 50% water and 50% ethylene glycol. In another study, Al-Mdallal et al. [40] explored the simultaneous effects of an inclined magnetic field and thermal radiation on Marangoni convection of a hybrid nanofluid, revealing significant changes in thermal boundary layer characteristics. Additional notable contributions to the understanding of energy transport in nanofluids can be found in the works of Renuka et al. [41] and Hussein et al. [27] each of which offers insights into the thermophysical interactions and enhancement mechanisms in magnetized or radiative nanofluid systems.

Although the present model extends prior formulations involving MHD nanofluid flow over moving surfaces, the originality of this study lies in its unified framework that combines a ternary hybrid nanofluid formulation with Joule heating, magnetic field and wall suction effects, which then solved numerically and analyzed statistically. Unlike previous works that rely on single-parameter variations, this study applies response surface methodology (RSM) with a central composite design (CCD) to evaluate the interaction effects and perform sensitivity analysis on the governing parameters. Moreover, the identification of optimal thermal conditions and critical design variables through ANOVA and regression model provides a statistically validated optimization strategy that has not been previously reported for ternary hybrid nanofluids in this configuration. Hence, the present study introduces a numerical and statistical investigation of MHD ternary hybrid nanofluid flow over a moving surface, integrating Joule heating, suction and magnetic field effects. By combining computational modeling with response surface-based optimization and sensitivity analysis, this research aims to establish an effective framework for improving heat transfer efficiency and flow stability. Ternary hybrid nanofluid comprising three distinct nanoparticles represents a cutting-edge advancement in thermal fluid technology, offering enhanced heat transfer rates, superior thermal conductivity, and improved stability as compared to the conventional and binary/ternary nanofluids. These unique properties make them highly relevant for practical applications in high-performance electronics cooling, solar thermal collectors, MHD pumps, biomedical drug delivery systems, heat exchangers and aerospace thermal shields, where efficient thermal control is essential under extreme or variable operating conditions. The novelty of this work lies in its unified approach to modeling, optimizing and analyzing MHD-driven ternary nanofluid flow using statistical tools, providing a valuable foundation for the design of next-generation thermal systems driven by multiphase transport phenomena.

Problem formulation

This study investigates the boundary layer flow and heat transfer characteristics of a ternary hybrid nanofluid composed of aluminum oxide/alumina, copper and titanium dioxide/titania or abbreviated as Al_2O_3, Cu and TiO_2 nanoparticles dispersed in water-based fluid over a moving surface. A Cartesian coordinate system is considered, where the x-axis lies along the surface while y-axis perpendicular to it into the fluid region $y \geq 0$. The free-stream velocity of the ternary hybrid nanofluid is maintained at a constant value U, while the velocity of the moving plate is characterized by λU, where λ is the velocity ratio parameter such that a positive λ indicates that the plate moves in the direction of the free stream, whereas a negative λ signifies motion against it. Besides, the physical model also incorporates the simultaneous effects of Joule heating and magnetic field, which arises from electrical resistive dissipation within the conducting nanofluid, influencing the temperature distribution across the boundary layer. The surface temperature T_w and the ambient temperature T_∞ are assumed to be constants. This configuration provides a platform for optimizing the heat transfer performance and performing sensitivity analysis on the influential physical parameters using response surface methodology (RSM).

Under the stated assumptions, the governing equations are derived based on the fundamental principles of momentum and energy conservation. These equations are suitably modified from existing formulations to accurately capture the flow behavior and heat transfer characteristics of the ternary hybrid nanofluid system, incorporating the effects of Joule heating, magnetic field and wall suction. The present model draws upon previous developments reported by Khashi'ie et al. [37] and Weidman et al. [42] to ensure consistency with boundary layer approximations and enhanced thermal transport modeling.

$$\text{Continuity equation}: \frac{\partial u}{\partial x} + \frac{\partial v}{\partial y} = 0, \tag{1}$$

$$\text{Momentum equation}: u\frac{\partial u}{\partial x} + v\frac{\partial u}{\partial y} = \frac{\mu_{\text{thnf}}}{\rho_{\text{thnf}}}\frac{\partial^2 u}{\partial y^2} - \frac{\sigma_{\text{thnf}}}{\rho_{\text{thnf}}}B^2(u-U), \tag{2}$$

$$\text{Energy equation}: u\frac{\partial T}{\partial x} + v\frac{\partial T}{\partial y} = \frac{k_{\text{thnf}}}{(\rho C_{\text{p}})_{\text{thnf}}}\frac{\partial^2 T}{\partial y^2} + \frac{\sigma_{\text{thnf}}}{(\rho C_{\text{p}})_{\text{thnf}}}B^2(u-U)^2, \tag{3}$$

$$\text{Boundary conditions: } u = \lambda U,\ v = v_{\text{w}},\ T = T_{\text{w}} \text{ at } y = 0,\ u \to U,\ T \to T_\infty \text{ as } y \to \infty. \tag{4}$$

Here, u and v are the velocity components along $x-$ axis and $y-$ axis, respectively, and $B = B_0 x^{-1/2}$ is the magnetic field equation, where B_0 is the magnetic field's strength (constant) (see Aly et al. [43]). The magnetic field is applied normal to the plate and align with $y-$ axis, while T is the ternary hybrid nanofluid's temperature. The mass flow at the surface is characterized by $v_{\text{w}} = -\sqrt{\frac{U v_{\text{f}}}{2x}}S$, where v_{w} represents the suction/injection velocity. The suction parameter S is introduced throughout the analysis to stabilize the boundary layer flow, particularly under reverse flow conditions. Table 1 presents the thermophysical property correlations for the ternary hybrid nanofluid, where ϕ_1,ϕ_2 and ϕ_3 represent the volumetric concentrations of Al_2O_3, Cu and TiO_2, respectively. Additionally, Table 2 summarizes the thermophysical properties of the base fluid and nanoparticles utilized in this study. Both Tables 1 and 2 are based on main references by Jamrus et al. [21–25].

Table 2 Thermophysical properties of the respective nanoparticles and water-based fluid

Physical properties	Al_2O_3	Cu	TiO_2	Water
$C_{\text{p}}/\text{J kg}^{-1}\text{ K}^{-1}$	765	385	686.2	4179
$\rho/\text{kg m}^{-3}$	3970	8933	4250	997.1
$k/\text{W m}^{-1}\text{ K}^{-1}$	40	400	8.9538	0.6130

The similarity transformations employed in this study are adapted from the formulations presented by Khashi'ie et al. [37] and Weidman et al. [42], ensuring consistency with boundary layer flow assumptions and the incorporation of physical effects such that

$$u = Uf'(\eta),\ v = \sqrt{\frac{U v_{\text{f}}}{2x}}(\eta f' - f),\ \eta = \sqrt{\frac{U}{2x v_{\text{f}}}}y,$$
$$\psi = \sqrt{2 v_{\text{f}} x U}f(\eta),\ \theta(\eta) = \frac{T - T_\infty}{T_{\text{w}} - T_\infty}. \tag{5}$$

By substituting the similarity transformations from Eq. (5) into the governing Eqs. 2–4, while ensuring the

Table 1 Correlations of thermophysical properties for hybrid nanofluids

Properties	Hybrid Nanofluid/*hnf* and Ternary Hybrid Nanofluid/*thnf*
Density	$\rho_{\text{hnf}} = (1-\phi_2)\left[(1-\phi_1)\rho_{\text{f}} + \phi_1\rho_{\text{s1}}\right] + \phi_2\rho_{\text{s2}}$ $\rho_{\text{thnf}} = (1-\phi_3)\left\{(1-\phi_2)\left[(1-\phi_1)\rho_{\text{f}} + \phi_1\rho_{\text{s1}}\right] + \phi_2\rho_{\text{s2}}\right\} + \phi_3\rho_{\text{s3}}$
Heat capacity	$(\rho C_{\text{p}})_{\text{hnf}} = (1-\phi_2)\left[(1-\phi_1)(\rho C_{\text{p}})_{\text{f}} + \phi_1(\rho C_{\text{p}})_{\text{s1}}\right] + \phi_2(\rho C_{\text{p}})_{\text{s2}}$ $(\rho C_{\text{p}})_{\text{thnf}} = (1-\phi_3)\left\{(1-\phi_2)\left[(1-\phi_1)(\rho C_{\text{p}})_{\text{f}} + \phi_1(\rho C_{\text{p}})_{\text{s1}}\right] + \phi_2(\rho C_{\text{p}})_{\text{s2}}\right\} + \phi_3(\rho C_{\text{p}})_{\text{s3}}$
Dynamic viscocity	$\frac{\mu_{\text{hnf}}}{\mu_{\text{f}}} = \frac{1}{(1-\phi_1)^{2.5}(1-\phi_2)^{2.5}}$ $\frac{\mu_{\text{thnf}}}{\mu_{\text{f}}} = \frac{1}{(1-\phi_1)^{2.5}(1-\phi_2)^{2.5}(1-\phi_3)^{2.5}}$
Thermal conductivity	$\frac{k_{\text{thnf}}}{k_{\text{hnf}}} = \left[\frac{k_{\text{s3}} + 2k_{\text{hnf}} - 2\phi_3(k_{\text{hnf}} - k_{\text{s3}})}{k_{\text{s3}} + 2k_{\text{hnf}} + \phi_3(k_{\text{hnf}} - k_{\text{s3}})}\right]$ where $\frac{k_{\text{hnf}}}{k_{\text{nf}}} = \left[\frac{k_{\text{s2}} + 2k_{\text{nf}} - 2\phi_2(k_{\text{nf}} - k_{\text{s2}})}{k_{\text{s2}} + 2k_{\text{nf}} + \phi_2(k_{\text{nf}} - k_{\text{s2}})}\right]$ $\frac{k_{\text{nf}}}{k_{\text{f}}} = \left[\frac{k_{\text{s1}} + 2k_{\text{f}} - 2\phi_1(k_{\text{f}} - k_{\text{s1}})}{k_{\text{s1}} + 2k_{\text{f}} + \phi_1(k_{\text{f}} - k_{\text{s1}})}\right]$
Electrical conductivity	$\frac{\sigma_{\text{thnf}}}{\sigma_{\text{hnf}}} = \left[\frac{\sigma_{\text{s3}} + 2\sigma_{\text{hnf}} - 2\phi_3(\sigma_{\text{hnf}} - \sigma_{\text{s3}})}{\sigma_{\text{s3}} + 2\sigma_{\text{hnf}} + \phi_3(\sigma_{\text{hnf}} - \sigma_{\text{s3}})}\right]$ where $\frac{\sigma_{\text{hnf}}}{\sigma_{\text{nf}}} = \left[\frac{\sigma_{\text{s2}} + 2\sigma_{\text{nf}} - 2\phi_2(\sigma_{\text{nf}} - \sigma_{\text{s2}})}{\sigma_{\text{s2}} + 2\sigma_{\text{nf}} + \phi_2(\sigma_{\text{nf}} - \sigma_{\text{s2}})}\right]$ $\frac{\sigma_{\text{nf}}}{\sigma_{\text{f}}} = \left[\frac{\sigma_{\text{s1}} + 2\sigma_{\text{f}} - 2\phi_1(\sigma_{\text{f}} - \sigma_{s1})}{\sigma_{\text{s1}} + 2\sigma_{\text{f}} + \phi_1(\sigma_{\text{f}} - \sigma_{\text{s1}})}\right]$

continuity condition described in Eq. (1) is satisfied, the following system of ordinary differential equations is derived:

$$\left(\frac{\mu_{\mathrm{thnf}}/\mu_{\mathrm{f}}}{\rho_{\mathrm{thnf}}/\rho_{\mathrm{f}}}\right)f''' + ff'' - \left(\frac{\sigma_{\mathrm{thnf}}/\sigma_{\mathrm{f}}}{\rho_{\mathrm{thnf}}/\rho_{\mathrm{f}}}\right)M\left(f' - 1\right) = 0, \tag{6}$$

$$\frac{1}{\mathrm{Pr}}\frac{k_{\mathrm{thnf}}/k_{\mathrm{f}}}{\left(\rho C_{\mathrm{p}}\right)_{\mathrm{thnf}}/\left(\rho C_{\mathrm{p}}\right)_{\mathrm{f}}}\theta'' + f\theta' + EcM\left(\frac{\sigma_{\mathrm{thnf}}/\sigma_{\mathrm{f}}}{\left(\rho C_{\mathrm{p}}\right)_{\mathrm{thnf}}/\left(\rho C_{\mathrm{p}}\right)_{\mathrm{f}}}\right)\left(f' - 1\right)^2 = 0, \tag{7}$$

$$\begin{aligned} &f'(0) = \lambda, f(0) = S, \theta(0) = 1, \\ &f'(\infty) = 1, \theta(\infty) = 0. \end{aligned} \tag{8}$$

The dimensionless parameters appearing in the transformed equations are defined as follows: M denotes the magnetic parameter, Pr represents the Prandtl number, and Ec corresponds to the Eckert number which accounts for the Joule heating. These parameters are mathematically defined as:

$$M = \frac{2\sigma_{\mathrm{f}}B_0^2}{U\rho_{\mathrm{f}}}, \ \mathrm{Pr} = \frac{\left(\mu C_{\mathrm{p}}\right)_{\mathrm{f}}}{k_{\mathrm{f}}}, \ \mathrm{Ec} = \frac{U^2}{\left(C_{\mathrm{p}}\right)_{\mathrm{f}}\left(T_{\mathrm{w}} - T_{\infty}\right)}. \tag{9}$$

The primary physical quantities of interest in this study are the skin friction coefficient C_{f} and the local Nusselt number Nu_{x}, which are defined as:

$$C_{\mathrm{f}} = \frac{\mu_{\mathrm{thnf}}}{\rho_{\mathrm{f}}U^2}\left(\frac{\partial u}{\partial y}\right)_{y=0}, \quad \mathrm{Nu}_{\mathrm{x}} = -\frac{xk_{\mathrm{thnf}}}{k_{\mathrm{f}}\left(T_{\mathrm{w}} - T_{\infty}\right)}\left(\frac{\partial T}{\partial y}\right)_{y=0}. \tag{10}$$

By applying the similarity transformations from Eq. (5) into Eq. (10), the simplified expressions for the skin friction coefficient and the local Nusselt number (representing the heat transfer coefficient) are obtained as follows:

$$\sqrt{2}Re_{\mathrm{x}}^{1/2}C_{\mathrm{f}} = \frac{\mu_{\mathrm{thnf}}}{\mu_{\mathrm{f}}}f''(0), \quad \sqrt{2}\mathrm{Re}_{\mathrm{x}}^{-1/2}Nu_{\mathrm{x}} = -\frac{k_{\mathrm{thnf}}}{k_{\mathrm{f}}}\theta\prime(0), \quad \mathrm{Re}_{\mathrm{x}} = xU/\nu_{\mathrm{f}}. \tag{11}$$

Results and discussion

The system of similarity equations presented in Eqs. 6, 7 and 8 is numerically solved to investigate the behavior of the skin friction coefficient $\sqrt{2}\mathrm{Re}_{\mathrm{x}}^{1/2}C_{\mathrm{f}}$ and the local Nusselt number $\sqrt{2}\mathrm{Re}_{\mathrm{x}}^{-1/2}\mathrm{Nu}_{\mathrm{x}}$ under the influence of various governing parameters. The numerical computation is then carried out using the MATLAB's built-in bvp4c solver, which is specifically designed for solving boundary value problems. The selection of the bvp4c solver in this study is justified by its superior handling of boundary value problems involving complex conditions. Unlike the shooting method which is highly sensitive to initial estimates and may struggle to capture multiple or dual solutions, bvp4c solver offers greater stability and reliability particularly when dealing with mixed boundary conditions. In contrast to traditional finite difference approaches, bvp4c includes an adaptive mesh refinement feature that enhances accuracy and computational efficiency. This solver requires an initial guess that satisfies the boundary conditions prescribed in Eq. (8) and iteratively refines the solution to achieve convergence within a predefined tolerance. The computational procedure begins with the conversion of the governing equations into a first-order system, as outlined in Eqs. 12–15, followed by appropriate coding of the system into the MATLAB software. Additional modifications are implemented during this step to ensure numerical stability and compatibility with the boundary constraints. The bvp4c solver is then employed to obtain the similarity solutions, facilitating a detailed evaluation of how physical parameters such as the magnetic field, Joule heating and nanoparticles concentration influence the thermal and momentum boundary layers.

$$f = y(1), f' = y(2), f'' = y(3), \theta = y(4), \theta' = y(5), \tag{12}$$

so that

$$f''' = \frac{\rho_{\mathrm{thnf}}/\rho_{\mathrm{f}}}{\mu_{\mathrm{thnf}}/\mu_{\mathrm{f}}}\left[\frac{\sigma_{\mathrm{thnf}}/\sigma_{\mathrm{f}}}{\rho_{\mathrm{thnf}}/\rho_{\mathrm{f}}}M(y(2) - 1) - y(1)y(3)\right], \tag{13}$$

$$\theta'' = \mathrm{Pr}\frac{(\rho C_{\mathrm{p}})_{\mathrm{thnf}}/(\rho C_{\mathrm{p}})_{\mathrm{f}}}{k_{\mathrm{thnf}}/k_{\mathrm{f}}}\left[-y(1)y(5) - \mathrm{Ec}M\left(\frac{\sigma_{\mathrm{thnf}}/\sigma_{\mathrm{f}}}{\left(\rho C_{\mathrm{p}}\right)_{\mathrm{thnf}}/\left(\rho C_{\mathrm{p}}\right)_{\mathrm{f}}}\right)(y(2) - 1)^2\right], \tag{14}$$

$$ya(1) - S, \ ya(2) - \lambda, \ ya(4) - 1, \ yb(2) - 1, \ yb(4). \tag{15}$$

Water was selected as the base fluid with Prandtl number $\mathrm{Pr} = 6.2$ due to its well-established thermal conductivity and favorable transport properties. The magnetic parameter, Eckert number and titania volumetric concentration are varied for the investigation of the nanofluid's behavior within these intervals $0.01 \le M \le 0.02$, $0 \le \mathrm{Ec}, \phi_3 \le 0.02$, while the concentrations of alumina and copper are fixed $\phi_1 = \phi_2 = 1\%$. The accuracy of the present numerical model was verified by comparing its results with benchmark solutions reported by Khashi'ie et al. [37] and Zainal et al. [44], as shown in Table 3. The close agreement between the computed values and existing literature confirms the validity and robustness of the proposed model in predicting ternary nanofluid heat and momentum transport characteristics. In addition, the numerical results (flow behavior and thermal performance) are graphically illustrated in Figs. 1–4. Notably, the results confirm the existence of dual solutions within specific parameter ranges; a characteristic often encountered in boundary layer flows over shrinking surfaces as shown in Table 4.

Table 3 Data validation of $f''(0)$ when $\phi_1 = 0$ (alumina), $\phi_2 = 0.1$ (copper) and $M = S = \phi_3 = \phi_4 = 0$

λ	Present		Khashi'ie et al. [37]		Zainal et al. [44]	
	First	Second	First	Second	First	Second
−0.2000	0.505318	0.026061	0.505318	0.026061	0.5053	0.0261
−0.2500	0.471688	0.053322	0.471688	0.053322	0.4717	0.0533
−0.3000	0.418959	0.099702	0.418959	0.099702	0.4190	0.0997
−0.3500	0.302592	0.209761	0.302592	0.209761	0.3028	0.2098

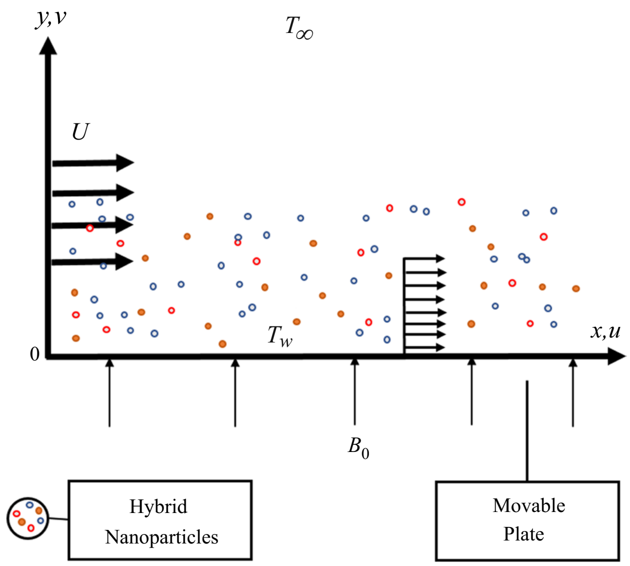

Fig. 1 Illustration of the physical model

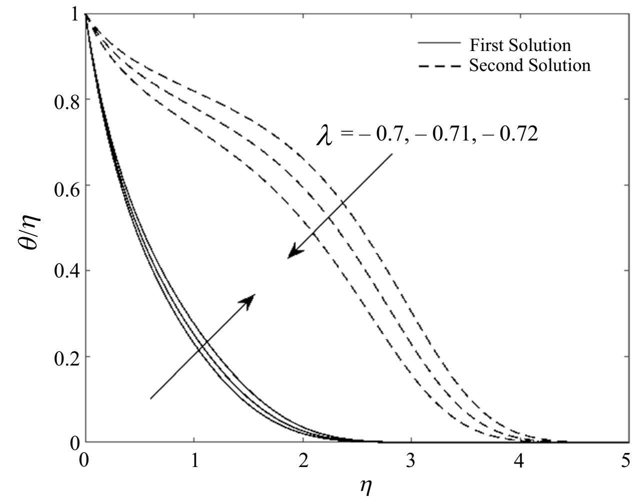

Fig. 3 Temperature profile with different λ when $M = Ec = 0.01$, $S = 0.5$, $\phi_1 = \phi_2 = \phi_3 = 1\%$ and Pr = 6.2

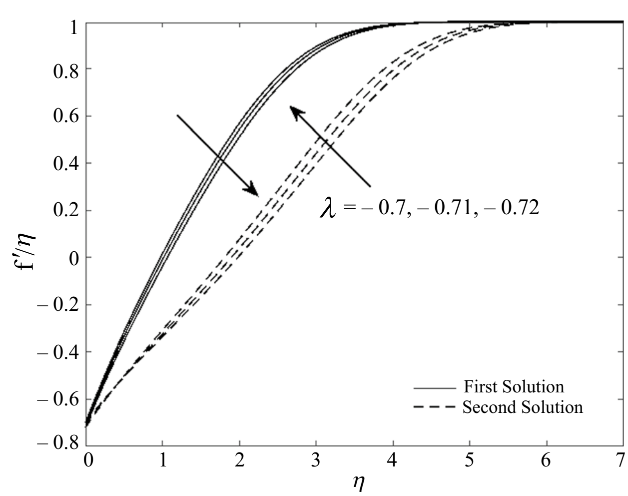

Fig. 2 Velocity profile with different λ when $M = Ec = 0.01$, $S = 0.5$, $\phi_1 = \phi_2 = \phi_3 = 1\%$ and Pr = 6.2

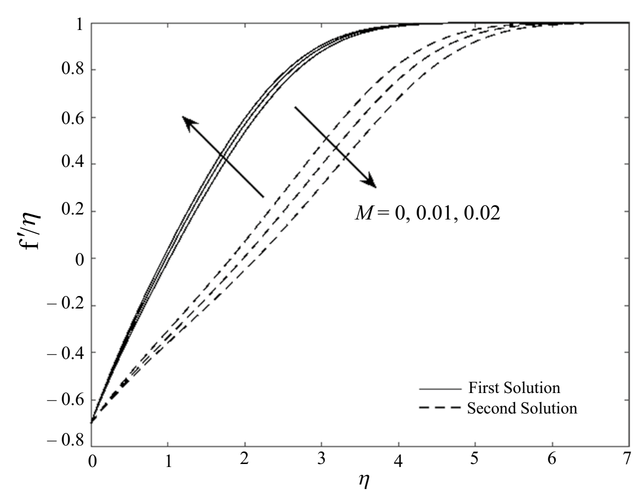

Fig. 4 Velocity profile with different M when $\lambda = -0.7$, $Ec = 0.01$, $S = 0.5$, $\phi_1 = \phi_2 = \phi_3 = 1\%$ and Pr = 6.2

The skin friction coefficient increases with stronger magnetic field intensity and higher titania concentration due to enhanced Lorentz force and increased effective viscosity, which together amplify momentum diffusion and suppress boundary layer separation. On the other hand, the Eckert number which quantifies the contribution of Joule heating does not significantly influence the flow velocity. In contrast, the heat transfer coefficient (Nusselt number) rises with increasing magnetic parameter as the induced Lorentz force

Table 4 Values of $\sqrt{2}\mathrm{Re}_x^{1/2}C_f$ and $\sqrt{2}\mathrm{Re}_x^{-1/2}\mathrm{Nu}_x$ for various values of M, Ec and ϕ_3 when $\phi_1 = \phi_2 = 0.01$, $S = 0.5$ and $\lambda = -0.7$

M	Ec	ϕ_3	$\sqrt{2}\mathrm{Re}_x^{1/2}C_f$		$\sqrt{2}\mathrm{Re}_x^{-1/2}\mathrm{Nu}_x$	
			First	Second	First	Second
0.01	0	0.01	0.92477	0.46912	1.93446	0.43332
	0.01		0.92477	0.46912	1.93268	0.42781
	0.02		0.92477	0.46912	1.93089	0.42230
0.02	0		0.96497	0.44845	1.97941	0.23920
	0.01		0.96497	0.44845	1.97601	0.22711
	0.02		0.96497	0.44845	1.97261	0.21502
0.01	0.01	0	0.89821	0.45771	1.93834	0.42535
		0.01	0.92477	0.46912	1.93268	0.42781
		0.02	0.95107	0.48100	1.92613	0.43120

stabilizes the flow and thins the thermal boundary layer, promoting enhanced thermal gradients at the wall. However, increasing either the Eckert number or titania concentration leads to a reduction in heat transfer rate. This behavior is attributed to the thermal load introduced by Joule heating (higher Eckert number), which raises the local fluid temperature and reduces the temperature difference driving heat flux. Similarly, a higher titania concentration increases the effective thermal capacity of the fluid, which can delay heat dissipation and lead to thicker thermal boundary layers. Consistent with prior studies, the first solution branch is known to represent the physically realizable and stable behavior, and thus, only the first solution is considered in the optimization process using response surface methodology (RSM), as described in the next section. These numerical results, obtained using the MATLAB's bvp4c solver, form the basis for the sensitivity and optimization analysis conducted in the subsequent sections.

Figures 2 and 3 depict the velocity and temperature distributions of the ternary hybrid nanofluid for various values of the moving parameter λ, while Figs. 3 and 4 illustrate the respective profiles under the influence of the magnetic parameter M. As depicted in Fig. 2, the velocity profile decreases with increasingly negative values of the moving parameter λ. This parameter defines the relative motion between the plate and the free stream. When $\lambda < 0$, it indicates that the plate moves in the opposite direction to the free stream. As the plate accelerates against the fluid motion (more negative λ), an adverse pressure gradient is introduced, which resists the flow development and suppresses the fluid velocity. This effect is characteristic of reverse flow behavior often seen in shrinking sheet problems. In contrast, Fig. 3 shows that the temperature profile increases with λ. Physically, when the plate moves strongly in the opposite direction to the ambient flow, the fluid experiences enhanced compressive effects, thickening the thermal boundary layer. This hinders the heat dissipation from the plate into the fluid and raises the local fluid temperature. Additionally, the suppression of fluid motion diminishes convective cooling, further contributing to thermal buildup in the boundary layer.

Figure 4 illustrates the variation in the velocity profile for different values of the magnetic parameter, considering only the first (stable) solution. Contrary to the conventional MHD cases involving forward stretching flow, the velocity profile here increases with increasing M. This behavior is attributed to the configuration of the current study, where the plate is moving opposite to the free stream $\lambda < 0$. In such a configuration, the application of a magnetic field induces a Lorentz force that, instead of opposing the flow, contributes to stabilizing and accelerating the near-wall fluid. This effect reduces backflow and enhances forward momentum, leading to a thicker boundary layer and an overall increase in velocity. The magnetic field thus plays a momentum augmentation role rather than a damping one under the influence of reverse surface motion. Meanwhile, Fig. 5 illustrates the temperature distribution of the ternary hybrid nanofluid for increasing values of the M, focusing solely on the first

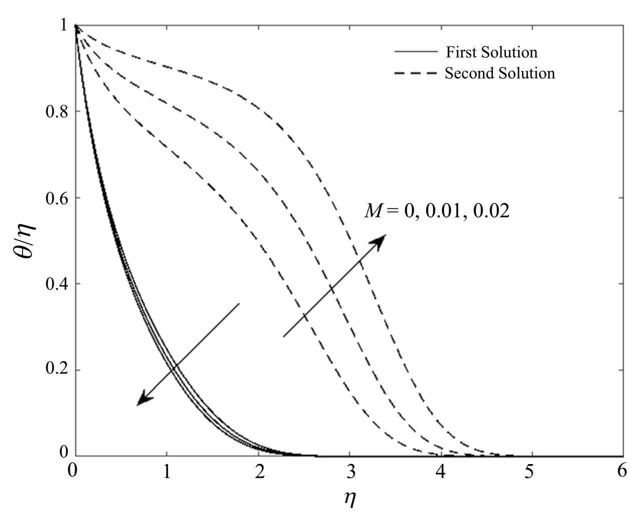

Fig. 5 Temperature profile with different M when $\lambda = -0.7$, $Ec = 0.01$, $S = 0.5$, $\phi_1 = \phi_2 = \phi_3 = 1\%$ and $\mathrm{Pr} = 6.2$

(stable) solution. It is observed that as the magnetic field strength increases from $M = 0$ to $M = 0.02$, the temperature profile increases. Physically, this behavior arises because the imposed magnetic field influences the flow structure in a way that enhances convective motion within the boundary layer for the first solution. As shown earlier in the velocity profile, the velocity increases with increasing M, which boosts the convective transport of thermal energy away from the surface.

Response surface and sensitivity analysis

This section delves into the response surface analysis performed on the numerical results obtained previously. The focus centers on examining how the governing parameters—magnetic parameter, Eckert number (for the Joule heating effect) and the titania volumetric concentration, affect the heat transfer and fluid flow behavior within the developed boundary layer model. By utilizing the response surface methodology (RSM), one kind of design of experiment (DOE), the study systematically explores these influences, enabling the identification of key factors that enhance critical responses such as the skin friction coefficient and the local Nusselt number. A central composite design (CCD) framework, embedded within the RSM, is employed to structure the experiments, as detailed in Table 5. The CCD consists of 20 simulation runs, with 3 independent variables: magnetic parameter (A), Eckert number (B) and titania concentration (C)—each investigated across three levels: low (–1), medium (0) and high (+ 1). This design ensures a robust and efficient exploration of the parameter space. The numerical data used in the RSM model are generated through the MATLAB's bvp4c solver, ensuring computational precision (refer to Table 4). The generalized response surface model (Eq. (16)) includes an intercept term $\left(r_0\right)$, linear terms reflecting individual parameter effects $\left(r_{\mathrm{A}}, r_{\mathrm{B}}, r_{\mathrm{C}}\right)$, quadratic terms capturing nonlinear responses $\left(r_{\mathrm{A}^2}, r_{\mathrm{B}^2}, r_{\mathrm{C}^2}\right)$ and interaction terms describing the coupled influences between variables $\left(r_{\mathrm{AB}}, r_{\mathrm{BC}}, r_{\mathrm{CA}}\right)$. Through this statistical modeling, the study provides deeper insights into the complex dynamics governing the ternary nanofluid system, aiding in the optimization of flow and thermal performance.

$$y = r_0 + r_{\mathrm{A}}\mathrm{A} + r_{\mathrm{B}}\mathrm{B} + r_{\mathrm{C}}\mathrm{C} + r_{\mathrm{AB}}\mathrm{AB} + r_{\mathrm{CA}}\mathrm{CA} + r_{\mathrm{BC}}\mathrm{BC} + r_{\mathrm{A}^2}\mathrm{A}^2 + r_{\mathrm{B}^2}\mathrm{B}^2 + r_{\mathrm{C}^2}\mathrm{C}^2 + \varepsilon. \tag{16}$$

Table 5 Experimental design

Run	Real			Coded				
	M	Ec	ϕ_3	A	B	C	Skin friction coefficient	Heat transfer coefficient
1	0.02	0	0.02	1	− 1	1	0.992277926	1.972943458
2	0.015	0.01	0.01	0	0	0	0.945475824	1.955496862
3	0.01	0	0.02	− 1	− 1	1	0.951066016	1.927947380
4	0.01	0.01	0.01	− 1	0	0	0.924774095	1.932676059
5	0.015	0.01	0.02	0	0	1	0.972285278	1.948945907
6	0.02	0.01	0.01	1	0	0	0.964973280	1.976008074
7	0.015	0.02	0.01	0	1	0	0.945475824	1.952885000
8	0.01	0.02	0	− 1	1	-1	0.898211936	1.936579037
9	0.015	0.01	0.01	0	0	0	0.945475824	1.955496862
10	0.015	0	0.01	0	− 1	0	0.945475824	1.958108724
11	0.015	0.01	0.01	0	0	0	0.945475824	1.955496862
12	0.015	0.01	0	0	0	− 1	0.918451917	1.961265311
13	0.02	0.02	0	1	1	− 1	0.937501668	1.978499496
14	0.01	0	0	− 1	− 1	− 1	0.898211936	1.940094553
15	0.015	0.01	0.01	0	0	0	0.945475824	1.955496862
16	0.01	0.02	0.02	− 1	1	1	0.951066016	1.924306634
17	0.02	0	0	1	− 1	− 1	0.937501668	1.985182593
18	0.015	0.01	0.01	0	0	0	0.945475824	1.955496862
19	0.02	0.02	0.02	1	1	1	0.992277926	1.966010795
20	0.015	0.01	0.01	0	0	0	0.945475824	1.955496862

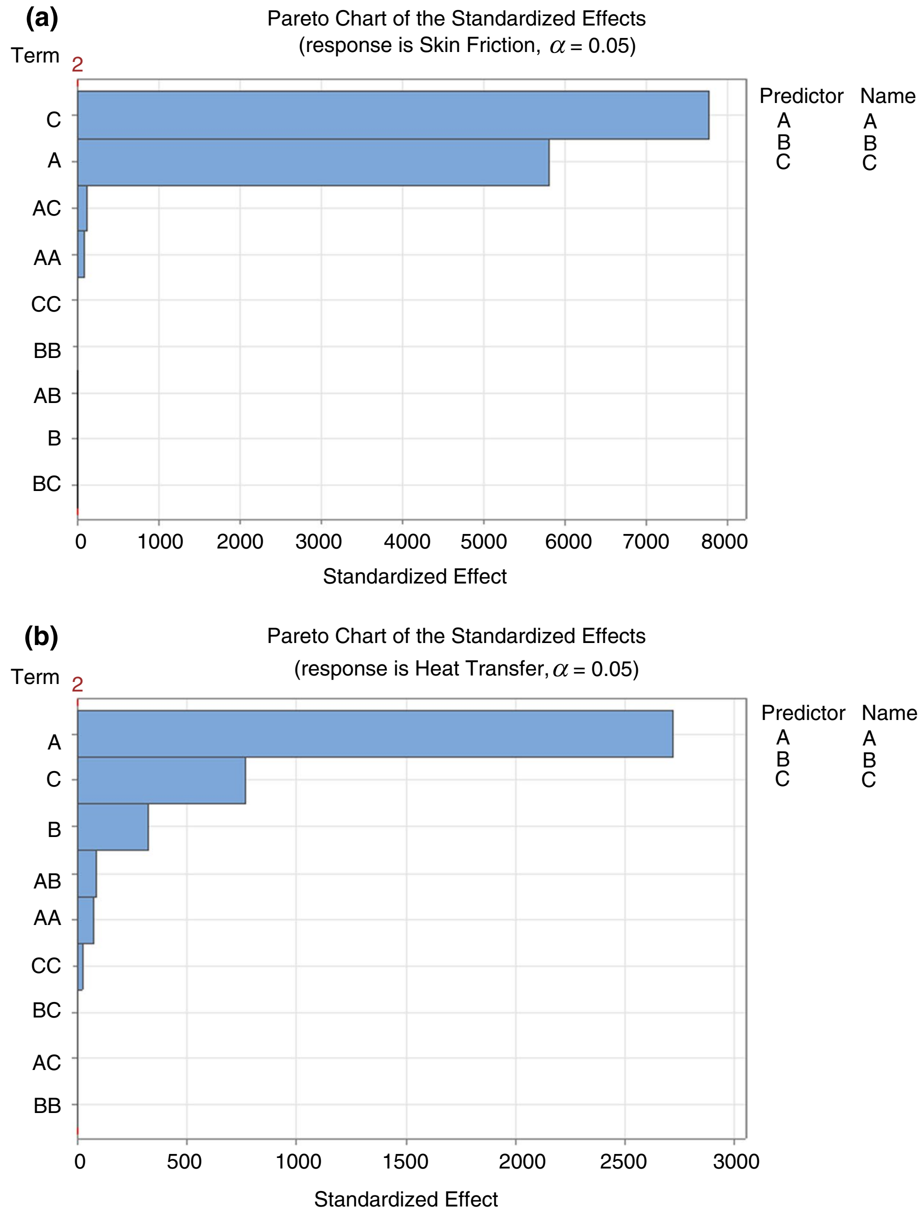

Fig. 6 Impact of the evaluated parameters using statistical data analysis on **a** skin friction coefficient and **b** heat transfer rate

Figure 6 presents standardized Pareto charts illustrating the influence of each design parameter on (a) skin friction coefficient and (b) Nusselt number at a 95% confidence level. For skin friction, term C has the greatest impact, followed closely by term A. The interaction term AC also shows a notable effect, while the remaining terms (AA, CC, BB, AB, B, BC) have much smaller standardized effects, indicating they are less significant in influencing skin friction. In contrast, for heat transfer, term A has the most significant effect, followed by term C and then term B. The other terms (AB, AA, CC, BC, AC, BB) have relatively minor effects, suggesting that they play a lesser role in affecting heat transfer. Overall, these charts help prioritize the factors and interactions that are most critical when analyzing or optimizing skin friction and heat transfer. They highlight that terms A and C are key contributors in both cases, although their relative importance varies depending on the specific response.

The models for the responses (skin friction and heat transfer rate), which account for both main/individual effects and their interactions, are given by the regression equations

$$y_{\text{skin friction}} = 0.945476 + 0.020120\text{A} + 0.000000\text{B} + 0.026909\text{C} - 0.000603\text{A}^2 - 0.000001\text{B}^2 - 0.000108\text{C}^2 + 0.000481\text{AC}, \quad (17)$$

Table 6 ANOVA for the skin friction coefficient

Source	DF	Adj SS	Adj MS	*F*-value	*P* value
A	1	0.004048	0.004048	33,713,782.86	0.000
B	1	0.000000	0.000000	0.00	1.000
C	1	0.007241	0.007241	60,304,402.95	0.000
A*A	1	0.000001	0.000001	8324.36	0.000
B*B	1	0.000000	0.000000	0.01	0.911
C*C	1	0.000000	0.000000	267.03	0.000
A*B	1	0.000000	0.000000	0.00	1.000
A*C	1	0.000002	0.000002	15,385.02	0.000
B*C	1	0.000000	0.000000	0.00	1.000
Error	10	0.000000	0.000000		
Lack-of-Fit	5	0.000000	0.000000	*	*
Pure error	5	0.000000	0.000000		
Total	19	0.011294			

$$y_{\text{heat transfer}} = 1.95550 + 0.021704\text{A} - 0.002600\text{B} - 0.006147\text{C} - 0.001157\text{A}^2 - 0.000002\text{B}^2 - 0.000393\text{C}^2 - 0.000807\text{AB} - 0.000039\text{AC} - 0.000047\text{BC}. \quad (18)$$

The sensitivity analysis is formulated by partially differentiating the response function from Eqs. (17) and (18), resulting in the sensitivity functions expressed in Eqs. (19) and (20).

$$\frac{\partial(y_{\text{skin friction}})}{\partial \text{A}} = 0.020120 - 0.001206\text{A} + 0.000481\text{C},$$
$$\frac{\partial(y_{\text{skin friction}})}{\partial \text{B}} = -0.000002\text{B},$$
$$\frac{\partial(y_{\text{skin friction}})}{\partial \text{C}} = 0.026909 - 0.000216\text{C} + 0.000481\text{A}, \quad (19)$$

$$\frac{\partial(y_{\text{heat transfer}})}{\partial \text{A}} = 0.021704 - 0.002314\text{A} - 0.000807\text{B} - 0.000039\text{C},$$
$$\frac{\partial(y_{\text{heat transfer}})}{\partial \text{B}} = -0.002600 - 0.000004\text{B} - 0.000807\text{A} - 0.000047\text{C}, \quad (20)$$
$$\frac{\partial(y_{\text{heat transfer}})}{\partial \text{C}} = -0.006147 - 0.000786\text{C} - 0.000039\text{A} - 0.000047\text{B}.$$

Table 6 shows the ANOVA results for the skin friction coefficient, highlighting which factors significantly affect skin friction. Factor C has the strongest effect, with a very high F-value and a *P* value of 0.000, meaning it is highly significant. Factor A also has a strong and significant effect. The interaction between A and C is important as well, showing a significant combined effect. The quadratic terms for A and C (AA and CC) are also significant, indicating that their effects are not just linear. On the other hand, Factor B and its interactions have no significant impact on skin friction, as shown by very low *F*-values and high *P* values. The error in the model is very small, and the lack-of-fit test suggests the model fits the data well. Overall, Factors A and C, along with their interaction and quadratic effects, are the main contributors to skin friction, while Factor B is not important. Figure 7 shows the individual value plots for A and C. Both factors have a clear positive effect on skin friction, with values increasing as A or C increase. This pattern is consistent across different levels of the other factor, meaning A and C independently increase skin friction. The error bars show some variability, but the overall trends are clear. There is no strong evidence of interaction effects, as the trends remain parallel.

Table 7 shows the ANOVA results for heat transfer, highlighting the importance of different factors and their interactions. Factor A has the strongest effect, with a very high F-value and a *P* value of 0.000, meaning it greatly influences heat transfer. Factors C and B also have significant effects, with high *F*-values and *P* values of 0.000. The quadratic effects of A (AA) and C (CC) are significant, indicating that their impact is not just linear. However, the quadratic effect of B (BB) is not significant, showing that it does not meaningfully affect heat transfer in a nonlinear way. All interaction terms (AB, AC and BC) are significant, meaning the combined effects of these factors also influence heat transfer. Overall, Factors A, B and C significantly affect heat transfer, including their interactions and quadratic effects,

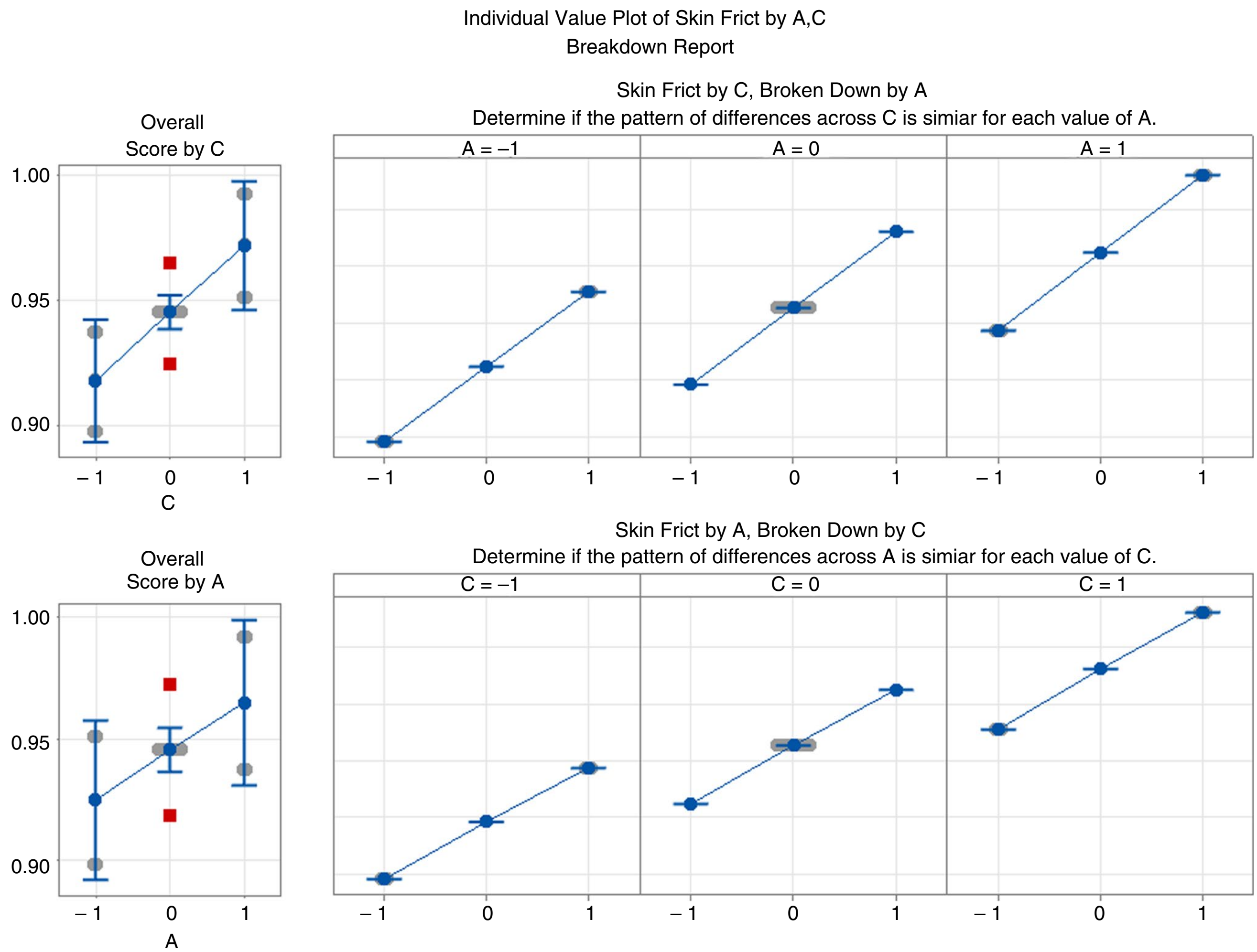

Fig. 7 Sensitivity analysis of A, B and C to skin friction

Table 7 ANOVA of the heat transfer

Source	DF	Adj SS	Adj MS	*F*-value	*P* value
A	1	0.004711	0.004711	7,396,300.87	0.000
B	1	0.000068	0.000068	106,105.17	0.000
C	1	0.000378	0.000378	593,216.78	0.000
A*A	1	0.000004	0.000004	5777.35	0.000
B*B	1	0.000000	0.000000	0.02	0.901
C*C	1	0.000000	0.000000	667.52	0.000
A*B	1	0.000005	0.000005	8189.16	0.000
A*C	1	0.000000	0.000000	18.65	0.002
B*C	1	0.000000	0.000000	27.57	0.000
Error	10	0.000000	0.000000		
Lack-of-Fit	5	0.000000	0.000000	*	*
Pure error	5	0.000000	0.000000		
Total	19	0.005172			

except for the quadratic effect of B, which is not important. The individual value plot in Fig. 8 shows the effects of A and C on heat transfer while keeping B constant. Factor A has a clear positive effect, with heat transfer increasing as A increases. Factor C shows a slight negative effect, with heat transfer decreasing a little as C increases. When looking at heat transfer by C at different levels of A (top row), the trend of decreasing heat transfer with increasing C is consistent, though there is some variability. Similarly, when examining heat transfer by A at different levels of C (bottom row), the positive effect of A remains clear and consistent, despite some variability. In summary, with B held constant, Factor A is the main driver of increased heat transfer, while Factor C has a smaller, slightly negative effect. The patterns suggest little interaction between A and C, as their effects remain fairly independent.

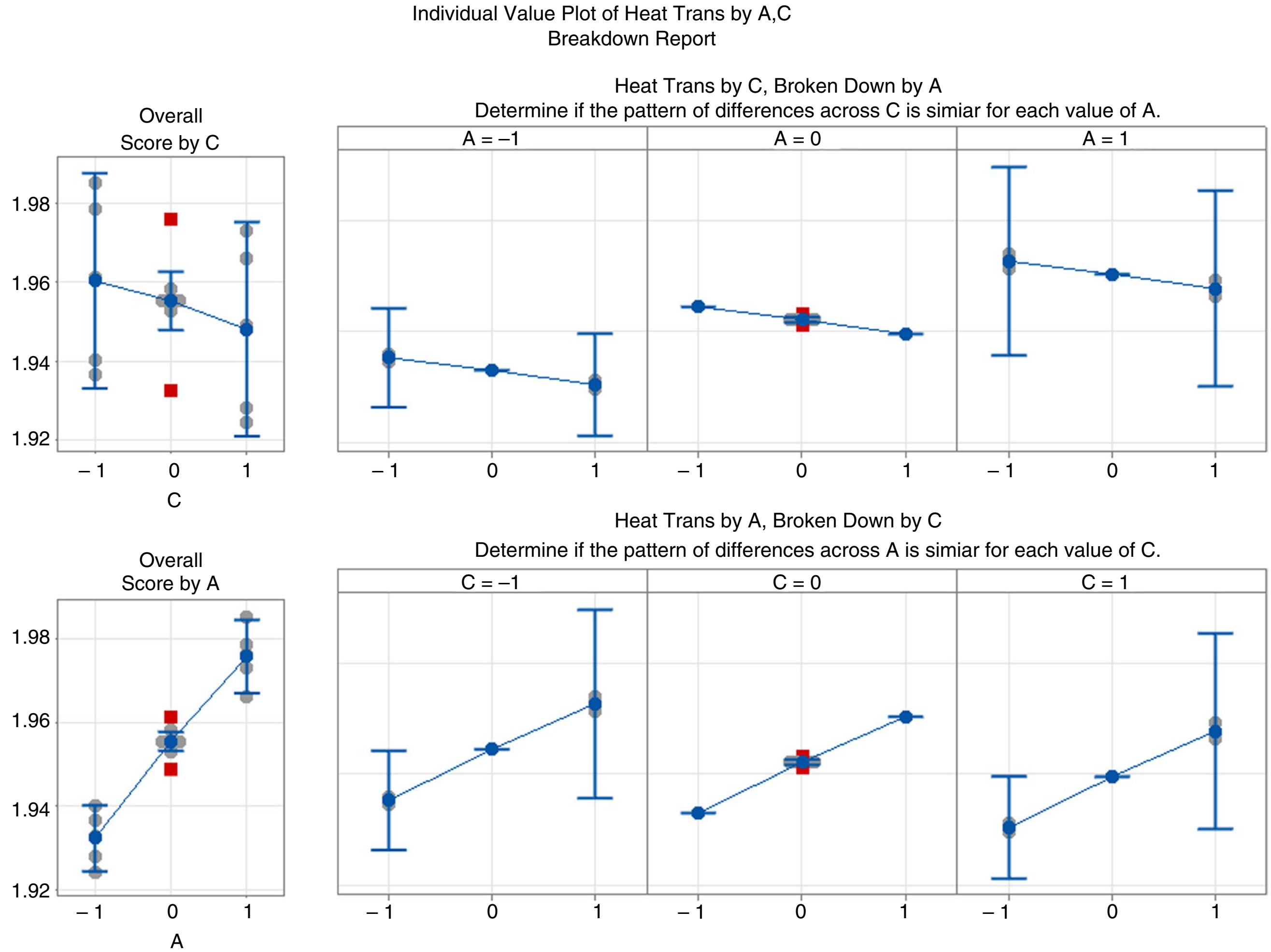

Fig. 8 Sensitivity analysis of A, B and C to heat transfer

Conclusions

This study provides a comprehensive numerical and statistical analysis of ternary hybrid nanofluid flow over a permeable moving surface incorporating the effects of Joule heating, magnetic field intensity and wall suction. The ternary hybrid nanofluid consisting of Al_2O_3, Cu and TiO_2 nanoparticles in a water base fluid demonstrates enhanced thermal and flow performance under the influence of key governing parameters. Numerical computation using the MATLAB bvp4c solver confirms that the magnetic parameter and titania concentration significantly enhance the velocity profile, while the Eckert number predominantly affects the temperature distribution. Suction plays a crucial role in stabilizing the flow, suppressing backflow and maintaining thermal efficiency. The integration of response surface methodology (RSM) and central composite design (CCD) provides a statistically robust platform for evaluating interaction effects and conducting sensitivity analysis. The ANOVA results confirm the magnetic parameter and titania concentration as the most influential variables in both skin friction and heat transfer responses. The developed regression models offer predictive insights into optimizing the flow and thermal characteristics of ternary hybrid nanofluid. Future work may extend this investigation in several cases:

1) Incorporating unsteady flow and time-dependent boundary conditions could provide a deeper understanding of transient thermal behavior in dynamic environments.
2) The inclusion of thermal radiation and chemical reactions could enrich the physical realism of the model.
3) Conducting experimental validation will be essential to confirm the numerical trends and enhance model reliability.
4) Extending the model to other geometries such as wavy or rotating surfaces would broaden its applicability to practical thermal systems in aerospace, biomedical and industrial cooling technologies.

Acknowledgements The research support is from Universiti Teknikal Malaysia Melaka (UTeM), Malaysia.

Author Contributions Umi Nadrah Hussein contributed to methodology, formal analysis and writing—original draft; Najiyah Safwa Binti Khashi'ie was involved in conceptualization, methodology, supervision and writing—review and editing; Mohd Fariduddin Mukhtar provided software (statistical analysis) and contributed to writing—review and editing; Norihan Md Arifin was involved in methodology, supervision, and writing—review and editing; and Ioan Pop contributed to supervision and writing—review and editing. All authors have read and agreed to the published version of the manuscript.

Funding Open access funding provided by The Ministry of Higher Education Malaysia and Universiti Teknikal Malaysia Melaka.

Declarations

Conflict of interest There is no conflict of interest.

References

1. Choi SUS, Eastman JA. Enhancing thermal conductivity of fluids with nanoparticles. ASME Fluids Eng Div. 1995;231:99–105.
2. Kamal M, Ali F, Khan N, Faizan M, Gul N, Muhammad T, et al. Second law analysis of two phase Maxwell mixed convective nanofluid using Marangoni flow and gyrotactic microorganism framed by rotating disk. J Therm Anal Calorim. 2025;150:1947–66.
3. Reddy MV, Pasha AA, Nath JM, Tirth V, Gupta P, Ansari MI, et al. Bioconvection flow and Hall current assessment on the Ree-Eyring nanofluid in the Darcy Forchheimer medium with irreversibility analysis. J Nonlinear Math Phys. 2025;32(1):31.
4. Reddy MV, Nath JM, Das TK, Ali F, Shah NA. Mixed convection flow on the Hall current effect of Ree-Eyring nanomaterial with gyrotactic microorganism and heat radiation flow. J Therm Anal Calorim. 2025;150:7731–51.
5. Shah NA, Ali F, Faizan M, Zafar SS. Theoretical exploration of bioconvection magneto flow of micropolar nanomaterial off-centered stagnation point framed by rotating disk. Adv Theory Simul. 2025;8(6):2401345.
6. Li S, Bilal M, Mir A, Kolsi L, Muhammad T, Ahmad Z. Parametric simulation of couple-stress nanofluid flow subject to thermal and solutal time relaxation factors. J Therm Anal Calorim. 2024;150:2393–406.
7. Ahmad Z, Crisci S, Murtaza S, Toraldo G. Numerical insights of fractal–fractional modeling of magnetohydrodynamic Casson hybrid nanofluid with heat transfer enhancement. Math Methods Appl Sci. 2024;47(11):9046–66.
8. Ali F, Kamal M, Ahmed MF, Zafar SS. Exact exploration of heat radiation and chemical reactive in the porosity flow of hybrid nanofluid using the laplace transform. ZAMM-J Appl Math Mech/Zeitschrift für Angewandte Mathematik und Mechanik. 2025;105(5):e70050.
9. Shah NA, Ali F, Yook SJ, Faizan M, Zafar SS, Sidi MO. Dynamics of chemical reactive on magneto Hybrid Nanomaterial with heat radiation due to porous exponential plate: laplace transform technique for the heat and mass. J Radiat Res Appl Sci. 2025;18(1):101295.
10. Gireesha BJ, Gowtham KJ. Thermal radiation impact on hybrid nanocomposite flow in stretchable channels: a Darcy-Forchheimer model with the Taylor wavelet approach. Appl Math Mech. 2025;46(6):1107–24.
11. Manvitha NV, Gireesha BJ, Gowtham KJ. Taylor wavelet solution procedure for the analysis of triangular porous fin made of functionally graded materials in the presence of hybrid nanofluid. Acta Mech. 2025;236:3055–80.
12. Lakshmi R, Gireesha BJ, Venkatesh P, Gowtham KJ. Hermite wavelet approach to analyze the entropy generation of MHD Williamson hybrid nanofluid flow through an inclined channel with particle shape effects. Int J Appl Comput Math. 2025;11(2):40.
13. Gireesha BJ, Gowtham KJ. Entropy generation analysis of hyperbolic tangent fluid in upright microchannel with Hall effect by Taylor wavelet collocation method. Int J Ambient Energy. 2025;46(1):2495825.
14. Manvitha NV, Gowtham KJ, Gireesha BJ. Physics informed neural network modeling and Fibonacci wavelet method for analyzing the efficiency of a magnetized cylindrical spine fin. Int Commun Heat Mass Transf. 2025;166:109151.
15. Gowtham KJ, Gireesha BJ. Enhancing efficiency in solving coupled Lane–Emden–Fowler equations with a novel Tricomi-Carlitz wavelet method. Z Angew Math Phys. 2025;76(2):52.
16. Kamal M, Faizan M, Ali F, Zafar SS, Ghachem K, Abdullah N, et al. Mixed convective flow caused by a porous vertical sheet in a Fourier heat fluxes for Darcy Forchheimer of biomedical simulation of Au-Cu/blood hybrid nanofluid. Case Stud Therm Eng. 2025;72:106233.
17. Zuberi HA, Lal M, Verma S, Chamkha AJ, Zainal NA. Impact of gold and silver nanoparticles injected in blood with viscous dissipation. Comput Methods Biomech Biomed Eng. 2025;28(8):1373–97.
18. Zuberi HA, Lal M, Singh A, Zainal NA, Chamkha AJ. Numerical simulation of blood flow dynamics in a stenosed artery enhanced by copper and alumina nanoparticles. Comput Model Eng Sci (CMES). 2025;142(2):1839–64.
19. Zainal NA, Mokhtar DM, Waini I, Zuberi HA, Nazar R, Pop I. Mixed convection of couple stress hybrid nanofluid past a vertical shrinking plate. J Therm Anal Calorim. 2025;150:8073–81.
20. Xuan Z, Zhai Y, Ma M, Li Y, Wang H. Thermo-economic performance and sensitivity analysis of ternary hybrid nanofluids. J Mol Liq. 2021;323:114889.
21. Jamrus FN, Waini I, Khan U, Ishak A. Effects of magnetohydrodynamics and velocity slip on mixed convective flow of thermally stratified ternary hybrid nanofluid over a stretching/shrinking sheet. Case Stud Therm Eng. 2024;55:104161.
22. Jamrus FN, Ishak A, Waini I, Khan U, Siddiqui MI, Madhukesh JK. Aspects of non-unique solutions for Hiemenz flow filled with ternary hybrid nanofluid over a stretching/shrinking sheet. Adv Math Phys. 2024;2024(1):7253630.
23. Jamrus FN, Ishak A, Waini I, Khan U, Hussain SM, Madhukesh JK, et al. Stability scrutinization of a non-Newtonian (Williamson) ternary hybrid nanofluid past a stretching/shrinking sheet.

ZAMM-J of Appl Math Mech/Zeitschrift für Angewandte Mathematik und Mechanik. 2025;105(2):e202300926.
24. Jamrus FN, Waini I, Khan U, Ishak A. Stagnation slip flow of ternary hybrid nanofluid over an exponentially shrinking/stretching sheet with Joule heating, MHD, and thermal radiation effects. Chin J Phys. 2025;94:518–39.
25. Jamrus FN, Waini I, Ishak A. Time-depending flow of ternary hybrid nanofluid past a stretching sheet with suction and magnetohydrodynamic (MHD) effects. J Adv Res Fluid Mech Therm Sci. 2024;117(2):15–27.
26. Hussein UN, Khashi'ie NS, Arifin NM, Pop I. Magnetohydrodynamics (MHD) flow of ternary nanofluid and heat transfer past a permeable cylinder with velocity slip. Chin J Phys. 2025;93:328–39.
27. Hussein UN, Khashi'ie NS, Hamzah KB, Arifin NM, Pop I. Joule heating effect on ternary nanofluid flow and heat transfer over a permeable cylinder. JP J Heat Mass Transf. 2024;37(6):831–41.
28. Mahboobtosi M, Hosseinzadeh K, Ganji DD. Investigating the convective flow of ternary hybrid nanofluids and single nanofluids around a stretched cylinder: parameter analysis and performance enhancement. Int J Thermofluids. 2024;23:100752.
29. Patil PM, Goudar B, Sheremet MA. Tangent hyperbolic ternary hybrid nanofluid flow over a rough-yawed cylinder due to impulsive motion. J Taibah Univ Sci. 2023;17(1):2199664.
30. Murtaza S, Becheikh N, Rahman AU, Sambas A, Maatki C, Kolsi L, et al. Thermal performance analysis of a nonlinear couple stress ternary hybrid nanofluid in a channel: a fractal-fractional approach. Nanomaterials. 2024;14(22):1855.
31. Lakshmi R, Gireesha BJ, Venkatesh P, Gowtham KJ. Irreversibility analysis of Carreau trihybrid nanofluid flow in a vertical microchannel under hall effect: a hypergeometric wavelet approach. Multiscale Multidiscip Model Exp Des. 2025;8(8):357.
32. Reddy MG, Reddy KV. Influence of Joule heating on MHD peristaltic flow of a nanofluid with compliant walls. Procedia Eng. 2015;127:1002–9.
33. Maskeen MM, Zeeshan A, Mehmood OU, Hassan M. Heat transfer enhancement in hydromagnetic alumina–copper/water hybrid nanofluid flow over a stretching cylinder. J Therm Anal Calorim. 2019;138:1127–36.
34. Khashi'ie NS, Arifin NM, Pop I, Wahid NS. Flow and heat transfer of hybrid nanofluid over a permeable shrinking cylinder with Joule heating: a comparative analysis. Alexandria Eng J. 2020;59(3):1787–98.
35. Yan L, Dero S, Khan I, Mari IA, Baleanu D, Nisar KS, et al. Dual solutions and stability analysis of magnetized hybrid nanofluid with joule heating and multiple slip conditions. Processes. 2020;8(3):332.
36. Chamkha AJ, Dogonchi AS, Ganji DD. Magneto-hydrodynamic flow and heat transfer of a hybrid nanofluid in a rotating system among two surfaces in the presence of thermal radiation and Joule heating. AIP Adv. 2019;9:025103.
37. Khashi'ie NS, Arifin NM, Pop I. Magnetohydrodynamics (MHD) boundary layer flow of hybrid nanofluid over a moving plate with Joule heating. Alexandria Eng J. 2022;61(3):1938–45.
38. Li Z, Shafee A, Kandasamy R, Ramzan M, Al-Mdallal QM. Nanoparticle transportation through a permeable duct with Joule heating influence. Microsyst Technol. 2019;25:3571–80.
39. Saranya S, Al-Mdallal QM, Javed S. Shifted legendre collocation method for the solution of unsteady viscous-ohmic dissipative hybrid ferrofluid flow over a cylinder. Nanomaterials. 2021;11(6):1512.
40. Al-Mdallal QM, Indumathi N, Ganga B, Hakeem AA. Marangoni radiative effects of hybrid-nanofluids flow past a permeable surface with inclined magnetic field. Case Stud Therm Eng. 2020;17:100571.
41. Renuka A, Muthtamilselvan M, Al-Mdallal QM, Doh DH, Abdalla B. Unsteady separated stagnation point flow of nanofluid past a moving flat surface in the presence of Buongiorno's model. J Appl Comput Mech. 2021;7(3):1283–90.
42. Weidman PD, Kubitschek DG, Davis AM. The effect of transpiration on self-similar boundary layer flow over moving surfaces. Int J Eng Sci. 2006;44(11–12):730–7.
43. Aly EH, Benlahsen M, Guedda M. Similarity solutions of a MHD boundary-layer flow past a continuous moving surface. Int J Eng Sci. 2007;45(2–8):486–503.
44. Zainal NA, Nazar R, Naganthran K, Pop I. MHD flow and heat transfer of hybrid nanofluid over a permeable moving surface in the presence of thermal radiation. Int J Numer Methods Heat Fluid Flow. 2021;31(3):858–79.